PNAS RESEARCH ARTICLE | CHEMISTRY

Cooperative redox and spin activity from three redox congeners of sulfur-bridged iron nitrosyl and nickel dithiolene complexes

Manuel Quiroz[a], Molly M. Lockart[b], Mohamed R. Saber[c], Shaik Waseem Vali[d], Lindy C. Elrod[a], Brad S. Pierce[e], Michael B. Hall[a], and Marcetta Y. Darensbourg[a,1]

Contributed by Marcetta Darensbourg; received January 22, 2022; accepted May 6, 2022; reviewed by James Donahue, Dennis Lichtenberger, and Jonas Peters

The synthesis of sulfur-bridged Fe–Ni heterobimetallics was inspired by Nature's strategies to "trick" abundant first row transition metals into enabling 2-electron processes: redox-active ligands (including pendant iron–sulfur clusters) and proximal metals. Our design to have redox-active ligands on each metal, NO on iron and dithiolene on nickel, resulted in the observation of unexpectedly intricate physical properties. The metallodithiolate, $(NO)Fe(N_2S_2)$, reacts with a labile ligand derivative of $[Ni^{II}(S_2C_2Ph_2)]^0$, Ni_{DT}, yielding the expected S-bridged neutral adduct, FeNi, containing a doublet $\{Fe(NO)\}^7$. Good reversibility of two redox events of FeNi led to isolation of reduced and oxidized congeners. Characterization by various spectroscopies and single-crystal X-ray diffraction concluded that reduction of the FeNi parent yielded $[FeNi]^-$, a rare example of a high-spin $\{Fe(NO)\}^8$, described as linear $Fe^{II}(NO^-)$. Mössbauer data is diagnostic for the redox change at the $\{Fe(NO)\}^{7/8}$ site. Oxidation of FeNi generated the $2[FeNi]^+ \rightleftharpoons [Fe_2Ni_2]^{2+}$ equilibrium in solution; crystallization yields only the $[Fe_2Ni_2]^{2+}$ dimer, isolated as PF_6^- and $BArF^-$ salts. The monomer is a spin-coupled diradical between $\{Fe(NO)\}^7$ and Ni_{DT}^+, while dimerization couples the two Ni_{DT}^+ via a Ni_2S_2 rhomb. Magnetic susceptibility studies on the dimer found a singlet ground state with a thermally accessible triplet excited state responsible for the magnetism at 300 K ($\chi_M T = 0.67$ emu·K·mol^{-1}, $\mu_{eff} = 2.31\ \mu_B$), and detectable by parallel-mode EPR spectroscopy at 20 to 50 K. A theoretical model built on an H_4 chain explains this unexpected low energy triplet state arising from a combination of anti- and ferromagnetic coupling of a four-radical molecular conglomerate.

designed synthesis | iron–nickel | redox/spin states | magnetism | theory

Significance

Nature's strategies for engendering redox activity in earth-abundant transition metals, permitting them to compete with noble metals as kings of catalysis, include the positioning of two or more metals in close proximity and the effects of electron-delocalizing, "noninnocent" molecular addenda such as pendant iron–sulfur clusters and dithiolenes. A bioinspired synthesis of complexes of iron and nickel has applied both strategies, as found in hydrogenase active sites: nitric oxide is used as a redox-active constituent on iron that is sulfur-bridged to a nickel dithiolene. Concomitant with minor structural changes that signify the loci of charge from added or removed electrons are impressive magnetic differences resulting from population of electronic states and spin coupling.

The facilitation of redox activity in first-row transition metal complexes by the delocalization effects of ligands is a well-accepted axiom of coordination chemistry. In this regard, nitrosyl (NO) and dithiolene ligands have served as paradigms for over 5 decades (1–5). Their transition metal complexes continue to be, in the prosaic vocabulary, a "promising strategy" toward the design of efficient catalysts for the electroconversion of abundant feedstock to useful commodities (6–9). A second strategy for promoting or engendering accessibility to redox processes in first-row transition metals is to position two metals in close proximity such that the burden of charge build-up as an electron is added or removed from the unit is buffered by adjacent metals. Such design properties are apparent in the active sites of redox metalloproteins such as the [NiFe]- and [FeFe]-hydrogenases (10). The makeup of these EAS also demonstrates extensive involvement of redox-active iron sulfur clusters in the hydrogenases, particularly the [4Fe-4S] cluster directly attached to the dirion subsite in the H cluster of [FeFe]-H_2ase (11). A natural bimetallic example that incorporates a dithiolene-type ligand is the molybdenum–copper carbon monoxide dehydrogenase, [MoCu]-CODH, the CO oxidation enzyme. A sulfide ligand bridges the two metals while the dithiolene (molybdopterin) bound to Mo tunes structure and redox properties (12, 13).

With recognition of such themes in the evolutionarily perfected biological electrocatalysts, synthetic inorganic chemists have thus been encouraged to use a building block approach to engineer such properties as expressed above into small molecules (14, 15). The full characterization of such hybrid models is expected to also serve as a guide to entirely new structure/bonding motifs, with interesting electronic and magnetic properties. While synthetic monometallic systems with elaborate π-delocalization as in metalloporphyrins have yielded insight regarding substituent effects on metal-centered reactivity (16), various reviews point to the lack of obvious relationships between catalyst metrics and the redox-active nature of ligands. As noted by Savéant and coworkers

Author contributions: M.Q., B.S.P., M.B.H., and M.Y.D. designed research; M.Q., M.M.L., M.R.S., S.W.V., and L.C.E. performed research; M.Q. contributed new reagents/analytic tools; M.Q., M.M.L., B.S.P., and M.B.H. analyzed data; M.Q., M.R.S., B.S.P., M.B.H., and M.Y.D. wrote the paper.

Reviewers: J.D., Tulane University; D.L., The University of Arizona; and J.P., California Institute of Technology.

The authors declare no competing interest.

[1]To whom correspondence may be addressed. Email: marcetta@chem.tamu.edu.

This article contains supporting information online at http://www.pnas.org/lookup/suppl/doi:10.1073/pnas.2201240119/-/DCSupplemental.

Published June 13, 2022.

(16) and reviewed by Queyriaux (17), the variety of ways the motifs may interact preclude naïve interpretations. Nevertheless, the full characterization of isolable redox levels involved at the beginning of catalytic cycles is helpful for interpreting subsequent steps. Although redox-active ligands installed on heterobimetallics might appear to afford even more complexities, the additional handles may contain, as they do in the case described below, reliable reporters on the electron distribution and polarization as redox changes take place.

Previously, we demonstrated that metallodithiolates derived from tetradentate, contiguous N_2S_2 chelates, MN_2S_2, are efficient bidentate, *cis*-dithiolate S-ligating traps of exogeneous metals (18). Good stability has been achieved for various S-bridged bimetallic and multimetallic complexes, including those with redox activity on both the metallodithiolate ligand and the receiver M′, exemplified in the $Fe_2(NO)_3$ complex shown in Fig. 1 (19). As the paradigm for possibilities of electronic and vibrational coupling enabled by bridging thiolate sulfurs, the three redox levels in (NO)Fe(bme-dame)•$Fe(NO)_2$ showed selective electron addition first to the electronically softer dinitrosyl iron unit [in Enemark–Feltham notation, the $\{Fe(NO)_2\}^{9/10}$ couple], and the second electron goes to the mononitrosyl iron site [accessing the $\{Fe(NO)\}^{7/8}$ couple]. The effect of such electronic speciation on magnetic and vibronic properties was monitored by magnetic susceptibility, Fourier transform infrared (FTIR), and single-crystal X-ray diffraction (SC-XRD) analyses. The hinge between the two units created by the bridging thiolates placed the two irons at 2.71 Å separation (Fig. 1) and engendered a low-spin configuration for the $\{Fe(NO)\}^7$–$\{Fe(NO)_2\}^9$ cationic diradical. The separation increased with subsequent reduction but with otherwise minimal structural difference in the framework. Nevertheless, in the two-electron reduced $S = 1$ species, the Fe(NO) center of the N_2S_2 metalloligand is displaced out of the N_2S_2 plane by more than 0.3 Å relative to the one-electron reduced species and became linearized. The cationic form of the $Fe_2(NO)_3$ complex exists within a thermodynamic well, materializing by self-assembly from various synthetic approaches. This complex was described as a nominal model of the 2Fe subsite in [FeFe]-H_2ase and indeed showed some ability as an HER electrocatalyst at the first reduction event (20).

Since the classic publication of Wang and Stiefel in 2001 (21), there has been development of metal dithiolenes as catalysts and for applications to devices utilizing their optical, magnetic, and conductive properties (21–23). Pursuant of our program in metallodithiolates as ligands to appropriate receivers, we saw opportunity for the synthesis of heterobimetallic complexes of nickel dithiolenes according to the following strategy. A 2017 report by Donahue and coworkers introduced a synthon that provides entry to heteroleptic, square planar nickel and palladium dithiolenes that contain phosphine, isonitrile, and amine ligands and avoids higher S-bridged aggregates (24–27). With the expectation that an analogous synthetic strategy might yield stable molecules rich in

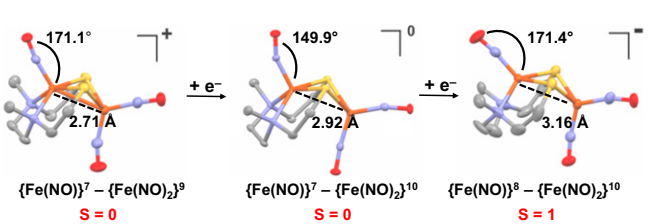

Fig. 1. Redox activity and magnetism properties of the $Fe_2(NO)_3$ complex in its three redox levels: singlet cation (*Left*), neutral doublet (*Middle*), and triplet anion (*Right*) (19).

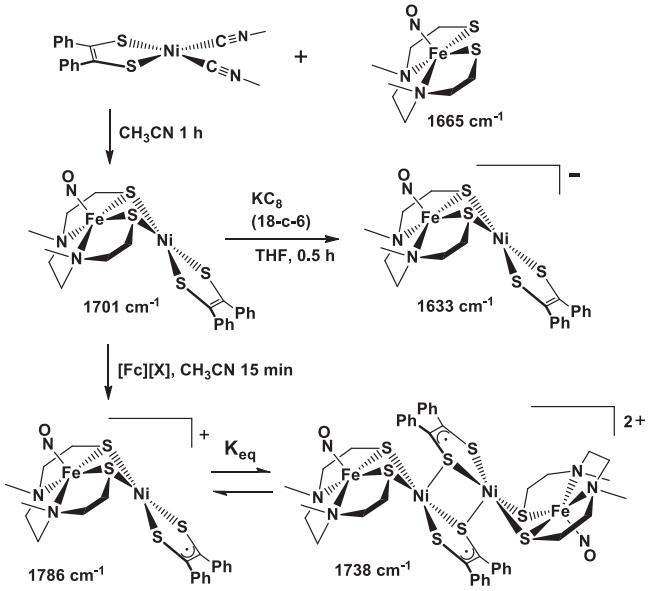

Fig. 2. Synthesis of **FeNi**, $[Fe_2Ni_2]^{2+}$, and $[FeNi]^-$ [ν(NO) values recorded from CH_3CN solutions]. For the oxidation using Fc^+, X = PF_6^- or $BArF^-$.

redox levels in hybrid dithiolene/nitrosyl complexes, we have pursued heterobimetallic nickel dithiolenes by replacing the traditional ligands such as phosphines or isonitriles with (NO)Fe(bme-dame) (Fig. 2). In this manner, we expected to build redox activity on both the M in MN_2S_2 and the nickel dithiolene. The following report chronicles successes in achieving the synthetic targets as well as the characterization by SC-XRD, FTIR, Mössbauer, superconducting quantum interference device (SQUID), and electron paramagnetic resonance (EPR) spectroscopies of cationic, neutral, and anionic forms of $[(NO)Fe(N_2S_2)\text{-}Ni(S_2C_2Ph_2)]^{+/0/-}$ ($[FeNi]^+$, **FeNi**, and $[FeNi]^-$, respectively). Perhaps the most interesting result of this study is the intricate spin interactions resulting from dimerization of the oxidized cationic $[FeNi]^+$ diradical complex that produces a tetraradical dication whose solid-state structure displays a Ni_2S_2 rhombic core. Interpretation of the spin ladder of $[Fe_2Ni_2]^{2+}$ by density functional theory (DFT) computations was incomplete, but full configuration interaction (FCI) calculations on a simple linear H_4 chain model were effective to identify two missing spin states and the relative energies of all six spin states of the elaborate $[Fe_2Ni_2]^{2+}$ system.

Results and Discussion

Synthesis of Neutral FeNi. The (NO)Fe(bme-dame)-$NiS_2C_2Ph_2$ complex [bme-dame = *N*,*N*′-dimethyl-*N*,*N*′-bis(2-mercaptoethyl)-ethylenediamine] was prepared using the Donahue and coworkers strategy (Fig. 2) (25, 26). Similar to the displacement of the labile isomethylnitrile ligands by diimines, reaction with the nitrosylated iron dithiolate yielded the neutral bimetallic complex, **FeNi**. The loss of the R-CΞN infrared absorptions at 2,214 and 2,228 cm^{-1} concomitant with the shift of the ν(NO) band by 37 cm^{-1} to higher wavenumbers (in acetonitrile) is consistent with expectations of such metallodithiolate donor units to the diamagnetic $NiS_2C_2Ph_2$ receiver. Slow evaporation of the DCM solvent under anerobic conditions afforded XRD quality crystals.

Electrochemical Studies. The cyclic voltammogram (Fig. 3) of **FeNi** was recorded in CH_3CN solutions containing 0.1 M $[^tBu_4N][PF_6]$ as the supporting electrolyte at room temperature under argon and referenced to $Fc^{+/0}$ ($E_{1/2}$ = 0.0 V) as an internal

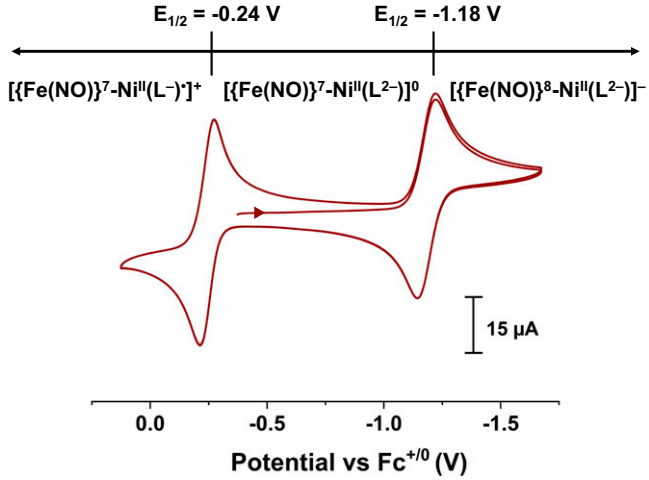

Fig. 3. Cyclic voltammogram of **FeNi** at a scan rate of 100 mVs^{-1} in CH_3CN (L = $S_2C_2Ph_2$). Referenced versus $Fc^{+/0}$.

standard. Commencing in the cathodic direction, **FeNi** has a reversible reduction at –1.19 V assigned to the $\{Fe(NO)\}^{7/8}$ couple; in the broader window an irreversible reduction at −2.53 V is ascribed to the $Ni^{II/I}$ couple. Scanning in the opposite direction shows an initial oxidation at −0.25 V assigned to the removal of an electron in the Ni-dithiolene unit denoted as $Ni_{DT}{}^{0/+}$. This reversible oxidation event shows a greater cathodic shift compared to most heteroleptic Ni-dithiolene complexes (26, 27). The reversible redox couples are confirmed to be one-electron events by comparison of current densities with the $Fc^{+/0}$ couple. Scanning further in the anodic region finds three irreversible redox events assumed to originate from sulfur-based oxidations and leads to overall decomposition. Full scans and scan rate dependence of **FeNi** are shown in *SI Appendix*, Figs. S14 and S15, respectively.

Chemical Oxidation and Reduction of FeNi. The fully reversible redox event at –0.25 V prompted attempts to isolate the oxidized form of **FeNi** by bulk chemical means. Oxidation using [Fc][BArF] ($BArF^-$ = Tetrakis[3,5-bis(trifluoromethyl)-phenyl]borate) or [Fc][PF_6] in CH_3CN at 23°C, led to loss of the 1,701 cm^{-1} band of the neutral species with appearance of two new ν(NO) bands at 1,786 and 1,736 cm^{-1} (Fig. 2). XRD quality crystals of the $BArF^-$ salt developed at –35°C from an Et_2O solution layered with pentane, while for the PF_6^- salt crystals were grown at –35°C from CH_3CN/Et_2O. In both salts, the crystal structures revealed that two **[FeNi]$^+$** cations have dimerized through the Ni-dithiolene units, **[Fe_2Ni_2][BArF]$_2$** and **[Fe_2Ni_2][PF_6]$_2$** (Fig. 4). That is, one dithiolene sulfur from each **[FeNi]$^+$** cation serves as a fifth donor toward each of the corresponding Ni^{II}, generating square pyramidal nickel within an Ni_2S_2 core for the dicationic **[Fe_2Ni_2]$^{2+}$** complex whose monomeric components are otherwise analogous to the neutral parent. This dimeric species has a solid-state ν(NO) value of 1,734 cm^{-1} indicating that the lower-frequency solution phase band at 1,736 cm^{-1} in CH_3CN corresponds to the dimeric species, while the band at 1,782 cm^{-1} is likely due to the monomeric form.

The reduction event at –1.19 V is also reversible, and **FeNi** succumbed to chemical reduction in THF on providing KC_8 as reductant (Fig. 2) in the presence of 18-crown-6 (18-c-6). A significant ν(NO) band shift of 68 cm^{-1} (from 1,701 to 1,633 cm^{-1}) indicates that the added electron went into the $\{Fe(NO)\}^7$ unit to give an $\{Fe(NO)\}^8$ configuration. Unlike our previously reported $\{Fe(NO)\}^8$ within the thermally unstable **[$Fe_2(NO)_3$]$^-$** anionic complex (Fig. 1), the **[FeNi]$^-$** is prepared and isolated at room temperature without degradation. XRD quality orange crystals of [K(18-c-6)]$^+$**[FeNi]$^-$** were obtained from CH_3CN layered with Et_2O at – 35°C.

Solid-State Structures of FeNi, [Fe_2Ni_2][BArF]$_2$, [Fe_2Ni_2][PF_6]$_2$, and [FeNi]$^-$. Metric parameters used to describe the crystal structures of the four complexes of this study are compiled in *SI Appendix*, Table S3. The butterfly-like molecular structure of **FeNi** shown in Fig. 4 originates from the orientation of the convergent, bridging sulfur lone pairs of the cis-dithiolates. The angle of intersection (hinge angle) of the S1–Fe1–S2 and S1–Ni1–S2 planes is 110.57°, somewhat smaller in comparison to similar MN_2S_2 bimetallic complexes where the receiver metal unit has a

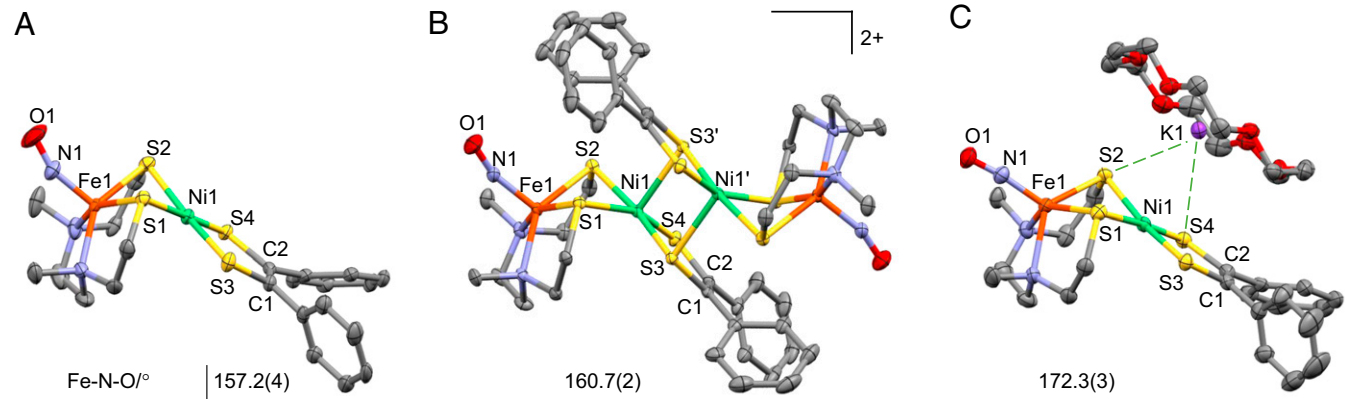

	A	B	C
Fe-N-O/°	157.2(4)	160.7(2)	172.3(3)
Fe···Ni/Å	2.7622(8)	2.9397(4)	3.0789(7)
Fe-N_2S_{2disp}/Å	0.568	0.554	0.859
Hinge/°	110.57	124.76	129.36
$S_3\cdots C_1$/Å	1.762(5)	1.726(3)	1.773(3)
$S_4\cdots C_2$/Å	1.759(4)	1.732(3)	1.759(4)
$C_1\cdots C_2$/Å	1.353(6)	1.369(3)	1.354(6)

Fig. 4. Molecular structures of (*A*) **FeNi**, (*B*) **[Fe_2Ni_2][PF_6]$_2$**, and (*C*) **[FeNi]$^-$** with thermal ellipsoids shown at 50% probability. The hydrogen atoms have been omitted for clarity. Selected structural metrics are shown. Fe–N_2S_{2disp} is the distance between Fe and the mean plane of the N_2S_2 ligand; the hinge is the angle of intersection between the S1–Fe1–S2 and S1–Ni1–S2 planes.

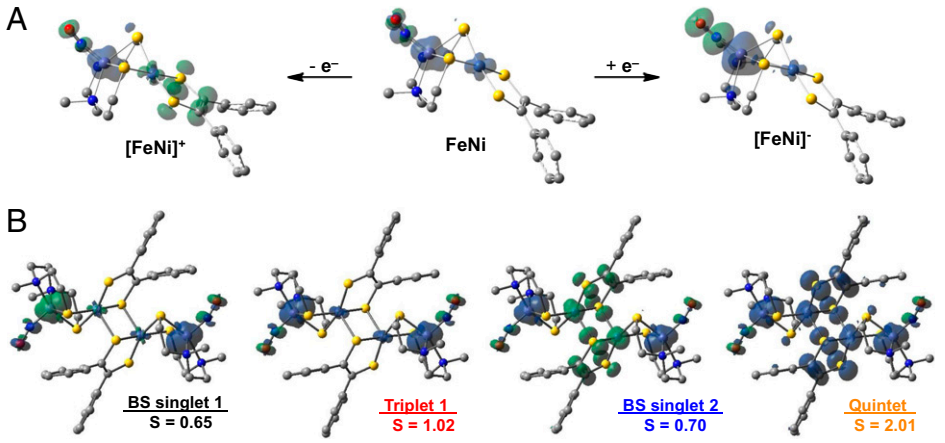

Fig. 5. (*A*) DFT computed spin density plots for the optimized ground state structures of the three monomeric redox congeners of **FeNi**. (*B*) Spin density plots and *S* values of $[Fe_2Ni_2]^{2+}$ obtained from single-point DFT calculations at its XRD structure The blue and green isodensity surfaces [0.004 e^- $Bohr^-$ (3)) indicate positive and negative spin phases, respectively.

higher coordination number. Notably, the smaller hinge angle correlates to a relatively short Fe–Ni distance of 2.76 Å.

Structural analyses of the nickel dithiolene unit, especially the S–C and C–C distances of the dithiolene, are informative of its redox level. The S3–C1 and S4–C2 distances for **FeNi** are 1.762(5) and 1.759(4) Å, respectively; the C1–C2 distance is 1.353 Å. These distances suggest that the ligand is a classical ene-1,2-dithiolate which resembles the reported $[Ni(S_2C_2Me_2)_2]^{2-}$ complex that has average S–C and C–C distances of 1.761 and 1.337 Å, respectively (28). Interestingly, the Fe-N-O angle changes only slightly from the free metallodithiolate (155.2° to 157.2°) although there is a 37 cm^{-1} difference in ν(NO). The latter shift is typical whenever the metalloligand is sharing its sulfur donors with an exogeneous metal (29), thereby withdrawing electron density from the Fe(NO), π-back-bonding interaction. Its paramagnetic spin state, $S = 1/2$, is, however, unchanged from the free $(NO)FeN_2S_2$ ligand and accounts for the overall magnetic moment of **FeNi** (vide infra).

Dissimilar space groups for the $BArF^-$ and PF_6^- salts of the oxidized product, $P\bar{1}$ and $P2_1/c$, respectively, result in slight differences, especially the S–Ni–S angles, within the Ni_2S_2 core (*SI Appendix*, Fig. S38) and have small effects on the Ni–Ni distance and the solid-state magnetism, vide infra.

Critical factors that distinguish the structures, including the hinge angle and M–M distance, are found in Fig. 4. For the reduced species, $[\mathbf{FeNi}]^-$, the increase in Fe–Ni distance and hinge angle is most pronounced, 0.317 Å and 18.79°, respectively. These differences relate to the Fe displacement from the N_2S_2 plane for the anionic form, which is 0.3 Å greater than that of the cationic and neutral forms. Such flexibility in ligand frameworks that accommodate reduction of iron-nitrosyl units has also been observed by Meyer and coworkers and Peters and Chalkley (30, 31)

Relative to the neutral **FeNi** species, the S3–C1 and S4–C2 distances within the dithiolene units on Ni in the cationic species, $[Fe_2Ni_2]^{2+}$, are diminished by an average of 0.033 Å, while the C1–C2 distance increased by an average 0.013 Å. Although small, these changes indicate the oxidized Ni-dithiolene unit is in the radical monoanion form (32). In contrast, the reduced species [where the added electron is on the Fe(NO) moiety, vide infra] experienced negligible changes in the Ni-dithiolene unit. The increased negative character in the $\{Fe(NO)\}^8$ unit is thus relayed to the thiolate sulfurs resulting in ion pairing from the S4 dithiolene sulfur and the adjacent metallodithiolate S2 sulfur toward the K^+ within the 18-c-6 adduct. Additional displays of this interaction, as well as electrostatic potential maps, are given in *SI Appendix*, Figs. S33 and S40.

DFT. Calculations are foundational for the discussion of electronic features and oxidation state assignments within the three Fe–Ni redox congeners. Experimental metric parameters were readily reproduced for **FeNi** and $[\mathbf{FeNi}]^-$ (*SI Appendix*, Table S8). Fig. 5*A* contains spin density plots from the optimized ground state structures. Neutral **FeNi** shows spin polarization in the $\{Fe(NO)\}^7$ unit with some leakage over to the Ni^{II}. Addition of an electron to yield the $S = 1$, $[\mathbf{FeNi}]^-$, puts even more density at the iron in $\{Fe(NO)\}^8$ with increased spin polarization. Removal of an electron from **FeNi** generates $[\mathbf{FeNi}]^+$ in the antiferromagnetically (AFM) coupled singlet ground state with unpaired spin of the opposite phase, compared to the iron, in a π orbital delocalized over the dithiolene radical cation with a small nickel contribution. Geometrically optimized computations predict that the broken symmetry (BS) singlet of the monomeric $[\mathbf{FeNi}]^+$ is more stable than the triplet state in THF by 1.76 kcal/mol. The BS singlet has spin contamination ($S = 0.3$) from the triplet excited state. Therefore, the approximate spin projection procedure was used on the ground state optimized structure to remove this error increasing the singlet–triplet gap to 3.8 kcal/mol (33, 34). The projected magnetic coupling constant (*J*) for the $\{Fe(NO)\}^7$ and nickel dithiolene interaction was calculated to be −665 cm^{-1} (34, 35).

This diradical dimerizes into a tetraradical dication whose magnetic properties provide an elaborate, four-electron system of potential spin couplings (Fig. 6) that yield six possible spin states: two singlets, three triplets, and a quintet. DFT calculations with the $[Fe_2Ni_2][BArF]_2$ XRD coordinates found only four single-determinant solutions for the dication. Those are a BS singlet ground state, a low-energy triplet, a high-energy BS singlet, and the high-energy quintet state (Fig. 5*B*). The two low-energy determinants (BS singlet 1 and triplet 1) feature an Ni_2S_2 core with two nickel dithiolene radicals that are strongly AFM coupled and show minor spin polarization. After correcting for spin contamination using the relatively uncontaminated triplet 1, the projected BS singlet ground state was found to be only 0.45 kcal/mol lower than that triplet 1; the apparent coupling between the $Fe(NO)^7$ radicals was calculated to be −77 cm^{-1}. The two higher-energy determinants are a BS singlet, which is contaminated by higher-energy spin states at +12.6, and a relatively

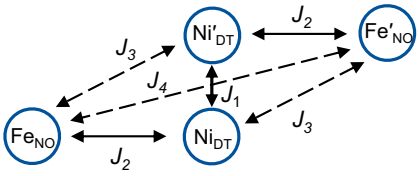

Fig. 6. The spin topology for $[Fe_2Ni_2]^{2+}$ with magnetic exchange pathways. $\{Fe(NO)\}^7$ and nickel dithiolene spin centers are denotated at Fe_{NO}/Fe'_{NO} and Ni_{DT}/Ni'_{DT}, respectively.

uncontaminated quintet at +17.1 kcal/mol above the projected energy of the ground state, respectively. The large energy difference between the low-energy determinants that have AFM Ni_2S_2 cores and the high-energy ones, where the nickel dithiolene radicals are not AFM coupled, indicates that the nickel dithiolene radicals are strongly AFM coupled in the dimer (estimated $J_1 \sim -2{,}500$ cm^{-1}). Based on the calculations, two $[FeNi]^+$ monomers with singlet ground states and relatively high-lying triplet states form a dimer which has a very low-lying triplet state. Such a situation arises for a particular combination of spin couplings in Fig. 6. Although each of these J values could contribute to the actual energy spacing of the six states, any two of their values are sufficient to produce six energetically different states.

Mössbauer Spectroscopy. The Enemark–Feltham notation is conveniently used in our iron nitrosyl descriptions, thus avoiding problematical oxidation state assignments in such delocalized metal-ligand systems. The series containing $\{Fe(NO)\}^{7/8}$ units within the $N_2S_2^{2-}$ ligand, **(NO)Fe(N_2S_2)** (N_2S_2 = bme-dame), the neutral heterobimetallic, **FeNi**, the anionic $[FeNi]^-$, and the dication $[Fe_2Ni_2][PF_6]_2$ gives prospect to expand the $[Fe_2(NO)_3]^{+/0/-}$ series explored earlier (19) and to make informed correlations between isomer shifts and redox levels of iron in similar first-coordination spheres. Fig. 7 displays the ^{57}Fe Mössbauer spectra and derived parameters.

All ^{57}Fe Mössbauer spectra exhibit a doublet at 5 K with a 0.05 T applied field. As a reference, the free ligand or **(NO)Fe(N_2S_2)** has an isomer shift (δ) of 0.27 mm s^{-1} and a quadrupole splitting (ΔE_Q) of 1.14 mm s^{-1}. Its binding to nickel in neutral **FeNi** results in little change in the δ value, 0.28 mm s^{-1}; however, the ΔE_Q significantly decreased to 0.75 mm s^{-1} and is ascribed to changes in electron density removed from the S donors to iron as they become the bridging bidentate ligands. Likewise, the oxidized product $[Fe_2Ni_2][PF_6]_2$ has similar δ and ΔE_Q values as the neutral **FeNi** analogue, 0.30 and 0.82 mm s^{-1}, respectively. Thus, the slight structural difference at the $(NO)FeN_2S_2$ component of the Fe–Ni complex resulting from the redox process centered in the Ni-dithiolene unit has negligible electronic effects on the oxidation state of iron that might be conveyed by the Mössbauer monitor. This conformity of Mössbauer parameters is notwithstanding the changes in π-back bonding from Fe to the diatomic ligand that results in a 37 cm^{-1} difference in the ν(NO), which parallels the loss of electron density to the Ni_{DT}. The most dramatic differences in δ and ΔE_Q occur in the reduced congener, the $[FeNi]^-$ anion, 0.73 and 2.33 mm s^{-1}, respectively. As this species shows the greatest change in structural factors relating to the Fe, we surmise that the increase in isomer shift reflects a lowered oxidation level centered on iron.

The correlation of Mössbauer isomer shifts and oxidation states of iron is notoriously difficult; values in the range 0.27 to 0.30 mm s^{-1} could correspond to both Fe^{III} or Fe^{II} centers when measured within an innocent ligand field (36). Relevant to the FeNi

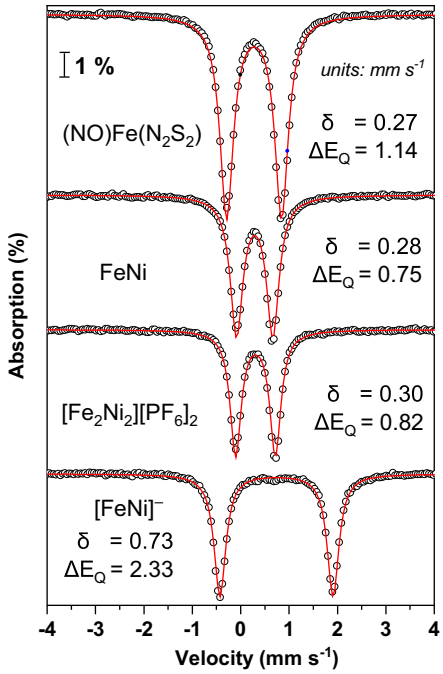

Fig. 7. The ^{57}Fe Mössbauer spectra of **(NO)Fe(N_2S_2)**, **FeNi**, $[Fe_2Ni_2][PF_6]_2$, and $[FeNi]^-$ collected as microcrystalline solids at 5 K with a 0.05 T applied field. Fits to the experimental data are shown in red with isomer shift and quadrupole splitting parameters given for each.

molecules here, the dianionic iron complex in $[Et_4N]_2$ $[ClFe(N_2S_2)]$ [where $N_2S_2^{4-}$ = *N,N′*-(2-thioacetyl-isobutyryl)-*o*-phenylene diamine] has the same square pyramidal geometry and a similar N_2S_2 ligand field to that found in (NO)Fe(bme-dame). It has an isomer shift of 0.292 mm s^{-1} at 4.3 K and was assigned as a Fe^{III}, S = 3/2, species (37). A recently reported bimetallic $[ClFe(bme\text{-}dame)\text{-}Cp^*Fe(CH_3CN)]^+$, in which the iron in the N_2S_2 ligand field with an apical, innocent Cl^- ligand is more obviously Fe^{III}, is particularly appropriate for comparison here. The zero-field Mössbauer spectrum at 80 K showed two doublets of equal intensity; the one with an isomer shift of 0.26 mm s^{-1} was assigned to the iron in the $N_2S_2^{2-}$ ligand field, i.e., the $ClFe^{III}$(bme-dame) metallodithiolate ligand (38). Consistent with this assignment, Popescu et al. (39) performed variable field Mössbauer studies on (NO)Fe(bme-dach) [bme-dach = *N,N*-bis(2-mercaptoethyl)-1,5-diazacycloheptane and δ = 0.23 mm s^{-1}] and argued for the assignment of an Fe^{III} oxidation state, in agreement with the analysis of Solomon and coworkers (40) of sulfur K-edge X-ray absorption spectroscopy on the analogous (NO)Fe(bme-daco) [bme-daco = *N,N*-bis(2-mercaptoethyl)-1,5-diazacyclooctane] complex.

As the above examples are so closely related to the $\{Fe(NO)\}^7$ units of our study, we conclude that the associated δ values are consistent with Fe^{III} centers in the neutral and cationic complexes. From published theoretical studies, including our own, the $\{Fe(NO)\}^7$ units can be best represented as overall doublets due to AFM coupling of intermediate-spin Fe^{III} (S = 3/2) and high-spin (S = 1) NO^-. Reduction to yield the $[FeNi]^-$ species should be based in the Fe(NO) component, to yield $\{Fe(NO)\}^8$. In this case the overall triplet results from AFM coupling of high-spin Fe^{II} (S = 2) and high-spin (S = 1) NO^-. The δ value of $[FeNi]^-$ (0.73 mm s^{-1}) differs from other reported high-spin $\{Fe(NO)\}^8$ examples, likely due to geometry and degree of covalency with the ligands (30, 41, 42). Again, recognizing the nature of the oxidation state construct is disputatious, particularly in these highly covalent $\{Fe(NO)\}^{7/8}$ units, our

formal oxidation state assignments gain credence from the agreement of spectroscopic and computational methods.

Monomer/Dimer Equilibria in Solutions of Oxidized FeNi. As described above, the two-ν(NO) IR band pattern observed in solution following oxidation of **FeNi** is associated with the presence of both the $[\mathbf{FeNi}]^{+}$ monomer and the dimeric $[\mathbf{Fe_2Ni_2}]^{2+}$. Assignment of the higher value to the former and the lower value to the asymmetric stretch of the two NO ligands in the latter is corroborated by the DFT results. Both ν(NO) bands display solvent-dependent shifts in position and in intensity (*SI Appendix*, Fig. S4). Differences in molar absorptivity coefficients (ε) could be determined as only the monomer is observed in THF solutions of 1.25 mM and less, thus permitting the unambiguous calculation of its ε. Through mass balance, the ε of the dimer was thus obtained and found to be ca. four times that of the monomer (see *SI Appendix* for details). Consequently, the equilibrium constant, K_{eq} as defined in Fig. 2, in THF was determined to be 26.7. The temperature dependence of K_{eq} in THF was used to obtain the ΔH° and ΔG° of dimer formation using the van't Hoff plot (*SI Appendix*, Fig. S18). As expected, dimer formation from two monomers at 23°C is a spontaneous process with a ΔG° of −1.9 kcal/mol and becomes more negative with decrease in temperature (*SI Appendix*, Table S1). The ΔH° and ΔS° of dimer formation were determined to be −6.72 kcal/mol and −16.2 cal/mol•K, respectively.

Magnetic Properties. Experimental determinations of magnetic properties of the FeNi bimetallic complexes in this study are as follows: 1) solution phase magnetism with NMR experiments to determine spin-only magnetic moments (μ_{eff}) using the Evans method or determination of singlet–triplet gaps by variable temperature ^{1}H NMR spectroscopy (43, 44), 2) EPR spectroscopy investigated in frozen solutions at low temperature, and 3) SQUID magnetometry measurements of the temperature dependence of the molar magnetic susceptibility from crystalline solids.

Solution phase magnetism (NMR methods). The Evans method data for **FeNi** and $[\mathbf{FeNi}]^{-}$ are shown in *SI Appendix*, Figs. S21 and S22. The μ_{eff} value for **FeNi** was determined to be 1.8 μ_B, and upon reduction to $[\mathbf{FeNi}]^{-}$, the magnetic moment increased to 3.1 μ_B consistent with triplet $\{Fe(NO)\}^8$ formation from doublet $\{Fe(NO)\}^7$. The singlet–triplet gap for monomeric $[\mathbf{FeNi}]^{+}$ was determined by using the Brown and coworkers (44) recent iteration of the variable temperature ^{1}H NMR spectroscopy method initially described by Cotton et al. (45). In our case we tracked the temperature dependence of the aromatic phenyl protons of the dithiolene ligand and saw nonlinear changes consistent with population of the excited triplet state (*SI Appendix*, Fig. S23). Our analysis of this data gave a singlet–triplet gap of about 6.9 kcal/mol corresponding to an exchange coupling constant (J) of –1,200 cm^{-1} for the AFM coupling of the $Ni_{DT}^{+\bullet}$ and $\{Fe(NO)\}^7$ radicals; this coupling is predicted by DFT (see *SI Appendix* for full details).

EPR spectroscopy. The X-band EPR measurements of both powder and solution samples of **FeNi** show isotropic spectra with $g = 2.02$ from the doublet $\{Fe(NO)\}^7$ unit (*SI Appendix*, Figs. S19 and 20). Both perpendicular- (9.64 GHz, ⊥) and parallel-mode (9.41 GHz, ∥) microwave field polarizations were used to perform EPR measurements on $[\mathbf{Fe_2Ni_2}]^{2+}$. Due to the poor solubility of $[\mathbf{Fe_2Ni_2}][\mathbf{PF_6}]_2$, samples of the $[\mathbf{Fe_2Ni_2}][\mathbf{BArF}]_2$ complex (10 mM) were prepared in diethyl ether/ethanol and slowly cooled to optimize the concentration of dimer over monomer. At 50 K, the sharp transition observed at $g = 2.0$ (circle in Fig. 8) is indicative of a minor amount (~0.17 mM) of free $(NO)Fe(N_2S_2)$ or neutral **FeNi** (Fig. 8). Quantitation of this signal accounts for (<2%) of the total complex in solution and thus will not be discussed further (its simulation parameters are provided in *SI Appendix*, Table S2). Significantly, the intensity of the $g \sim 4$ signal observed in parallel mode (Fig. 8, *Inset A*) deviates from Curie law behavior in that the temperature-normalized intensity (S × T) of the $g \sim 4$ signal increases with temperature. This indicates that the transition must originate from an excited doublet within a non-Kramer's spin system. Furthermore, the observed g value for this complex is diagnostic of a transition within an integer spin ($S = 1$) triplet manifold. Due to overparameterization for the proposed four-coupled spin system, the EPR data were treated as an isolated triplet state; this treatment is reasonable as the ground state singlet and low-energy triplet are well separated from the other spin states as discussed above. Within this simplified framework, the energy separating the ground |0> and excited state |±1> spin manifold represents the exchange coupling (J) between two equivalent $S = 1/2$ sites. This value was determined by fitting the temperature-normalized signal intensity (S × T) data to a Boltzmann population distribution for a two-level system (Eq. **4**) (*Materials and Methods*). As shown in Fig. 8, *Inset B*, the intensity of the $g \sim 4$ feature begins to plateau above 80 K suggesting the population of the excited |±1> spin manifold is approaching equilibrium. From this fit a minimum value for the magnitude of J_4 (-40 ± 7 cm^{-1}) was determined. In this model the two spin centers are the Fe_{NO} radicals which AFM couple through the Ni_2S_2 rhomb core. That is, the $Ni_{DT}^{+\bullet}$ radicals are so strongly coupled, as suggested by DFT, that a diamagnetic bridge is formed allowing superexchange between the Fe_{NO} units.

Among spin-coupled ($S = 1$) complexes, additional broad features flanking $g \sim 2$ can sometimes be observed in transverse mode providing $D < h\nu$ (46). As displayed in Fig. 8, similar signals for samples of $[\mathbf{Fe_2Ni_2}][\mathbf{BArF}]_2$ are observed at $g \sim$ 2.33, 2.16, 1.90, and 1.79. These broad peaks flanking the sharp $g = 2$ (circle in Fig. 8) signal originate from transitions within the |± 1> manifold and are highly diagnostic of the zero field splitting (ZFS) (47–49). The analytical EPR

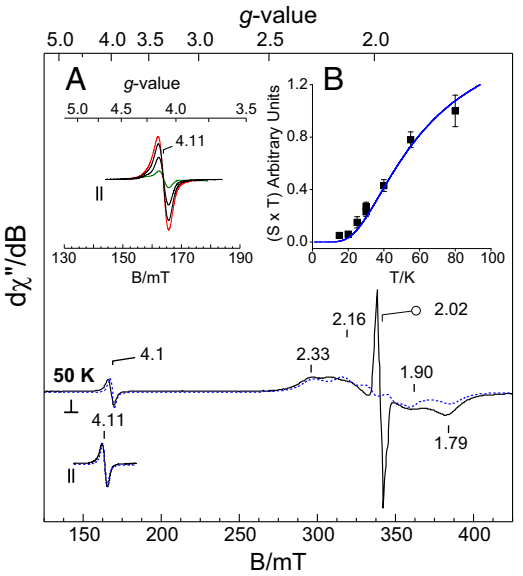

Fig. 8. X-band perpendicular (9.64 GHz) and parallel (9.41 GHz) mode CW EPR spectra of $[\mathbf{Fe_2Ni_2}][\mathbf{BArF}]_2$ collected at 50 K. (*Insets*) The parallel-mode $g \sim 4$ resonance at 20, 30, 40, and 50 K (*A*) and temperature-normalized (S × T) intensity of the parallel-mode resonance from 15 to 77 K (*B*). Instrumental parameters are as follows: microwave frequency, 9.41 GHz; microwave power, 21 mW; modulation amplitude, 0.98 mT.

simulations provided in Fig. 8 (dashed lines) were generated using the measured exchange coupling ($J_4 = -40$ cm^{-1}) established above. Here reasonable matches to all observed resonances in both perpendicular- and parallel-mode EPR were obtained assuming a small axial ZFS ($|D| = 0.05$ cm^{-1}) and nearly axial rhombicity ($E/D = 0.006$). The spectral line width was reproduced assuming only minor deviation of coupled system g values (2.02, 2.02, and 2.04) from the free-electron g value (g_e, 2.0023) and distributions in E/D ($\sigma_{E/D}$, 0.017). From this analysis, the concentration of **$[Fe_2Ni_2][BArF]_2$** determined by simulation is 12 ± 2 mM. Therefore, within error, the concentration of this triplet signal calculated by EPR simulation matches the amount of **$[Fe_2Ni_2][BArF]_2$** complex placed in solution.

SQUID magnetometry (direct current molar magnetic susceptibility). SQUID data were collected on powdered crystalline samples of **FeNi**, **$[Fe_2Ni_2][PF_6]_2$**, **$[Fe_2Ni_2][BArF]_2$**, and **$[FeNi]^-$** over a temperature range of 2 to 300 K under an applied field of 1,000 Oe. In accordance with the EPR spectrum of **FeNi**, the $\chi_M T$ value from SQUID measurements at 300 K is 0.39 emu K mol^{-1} corresponding to a low-spin $\{Fe(NO)\}^7$ (expected value for $S = 1/2$: 0.375 emu K mol^{-1}); it is essentially temperature independent (Fig. 9). For **$[FeNi]^-$** the room temperature $\chi_M T$ value of 1.23 emu K mol^{-1} is consistent with a triplet from the high-spin $\{Fe(NO)\}^8$ (Fig. 9). The $\chi_M T$ value remains nearly constant as the temperature is lowered until around 25 K where a steep $\chi_M T$ decrease is observed to give a minimum of 0.59 emu K mol^{-1}. The sharp decrease can be attributed to ZFS interactions. The temperature dependence of the $\chi_M T$ product over the 2 to 300 K range was fitted with the PHI software (50) using the spin Hamiltonian in Eq. **3** (*Materials and Methods*). Satisfactory fits were obtained using $g = 2.15$, $D = -15.3$ cm^{-1}, $E = \pm 0.9$ cm^{-1}, temperature-independent paramagnetic (TIP) = 2.4×10^{-4} emu·mol^{-1}. The field-dependent reduced magnetization data at temperatures between 1.8 and 4.5 K reveal nonsuperimposable isofield lines due to the presence of ZFS interactions (*SI Appendix*, Fig. S24) (51). Fits using ANISOFIT2.0 led to estimates of the axial ($D = -17$ cm^{-1}) and rhombic ($E = \pm 3.8$ cm^{-1}) ZFS parameters for **$[FeNi]^-$** with $g = 2.26$. These values are consistent with results obtained from PHI (52). The lack of saturation of the magnetization, even at 7 T, is not unexpected due to the anisotropic nature of the magnetic center but approaches the expected value of $\sim 2\ \mu_B$ (*SI Appendix*, Fig. S25). The D value of **$[FeNi]^-$** is about half of that found for **$[Fe(NO)_3]^-$** (-35 ± 3 cm^{-1}; Fig. 1) (19). This difference is likely due to the disparity in structural parameters for the $(NO)Fe(N_2S_2)$ unit; its τ value (a parameter for distinguishing square pyramidal and trigonal bipyramidal geometries) (53) in **$[FeNi]^-$** is 0.27 and that for **$[Fe(NO)_3]^-$** is 0.11 (i.e., the latter is less distorted from square pyramidal).

The $\chi_M T$ value is 0.67 emu K mol^{-1} at 300 K for **$[Fe_2Ni_2][PF_6]_2$** and gradually decreases as temperature is lowered with a steeper decrease at 100 K (Fig. 9); it is virtually zero below 20 K. This indicates that the dominant magnetic interaction of the four spin centers in **$[Fe_2Ni_2]^{2+}$** is AFM in character. However, as discussed in *EPR spectroscopy*, the simpler two-spin model was used to fit the SQUID data; the four-spin model is discussed in *A Simple Four-Spin Model*. To obtain an acceptable estimation of the magnitude of J_4, the susceptibility data were simulated using the Hamiltonian defined in Eq. **1**:

$$\hat{H} = -J_4(\hat{S}_1 \cdot \hat{S}_2). \qquad [1]$$

The expression corresponds to the Heisenberg–Dirac–van Vleck magnetic exchange where S_1 and S_2 are $\{Fe(NO)\}^7$ radical spins

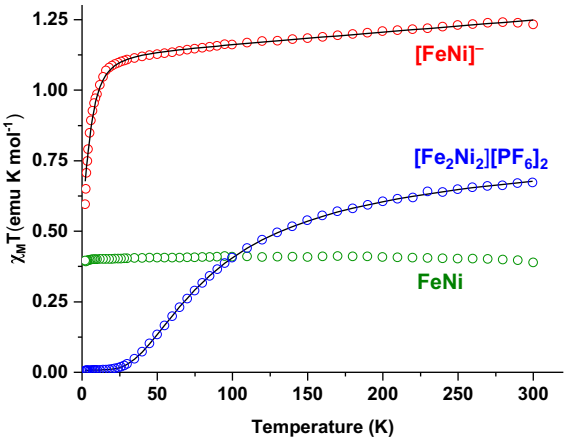

Fig. 9. Variable temperature magnetic susceptibility measurements for **FeNi** (green), **$[Fe_2Ni_2][PF_6]_2$** (blue), and **$[FeNi]^-$** (red) collected between 2 and 300 K with a 0.1 T field. Black lines are the fits.

($S = 1/2$). Satisfactory simulations were obtained using $g = 2$ and a coupling constant of $J_4 = -53.3$ cm^{-1}. Similar results were obtained ($J_4 = -37.5$ cm^{-1}) for the $BArF^-$ salt. These values closely match what was obtained from EPR spectroscopy. That is, for both methods the singlet–triplet energy gap is found to be ca. 0.2 to 0.3 kcal/mol.

A Simple Four-Spin Model. Hypothetically, a simple model of the **$[Fe_2Ni_2]^{2+}$** complex might elucidate where the missing states fit within the spin ladder of the six possible low-energy states of **$[Fe_2Ni_2]^{2+}$**. The simplest depiction of an actual molecular four-spin system is four hydrogen atoms in a row, so an $H_{4\ chain}$ molecule might serve as a model for **$[Fe_2Ni_2]^{2+}$**. The H_4 model contains two distances: R_1, the distance between the outer hydrogen atoms and their nearest inner neighbor, and R_2, the distance between the two inner hydrogen atoms ($H \overset{R_1}{\cdots} H \overset{R_2}{\cdots} H \overset{R_1}{\cdots} H$). To benchmark the R_1 distance, FCI calculations were performed on H_2 at various H–H distances until a distance was found where the singlet–triplet gap for H_2 was equal to the gap for the cation monomer, **$[FeNi]^+$**. Single-point calculations found the singlet–triplet gap for the **$[FeNi]^+$** fragment from the dimer XRD structure to be 4.2 kcal/mol, which is matched by an FCI at an H–H distance of 2.39 Å. The R_2 distance was benchmarked by setting the R_1 distances to 2.39 Å and scanning the R_2 distance until the energy between the ground state singlet (GSS) to the quintet state matched the DFT calculated value (~17 kcal/mol) from **$[Fe_2Ni_2]^{2+}$**, yielding an R_2 distance of 2.04 Å.

A comparison of the partial DFT spin ladder for **$[Fe_2Ni_2]^{2+}$** and the complete spin ladder for the linear H_4 model is shown in Fig. 10*A*. The H_4 model has a similar low-energy triplet at +0.90 kcal/mol compared to +0.45 kcal/mol for **$[Fe_2Ni_2]^{2+}$**. The high-energy BS singlet 2 in H_4 is slightly more stable than the related high-energy BS, $M_s = 0$ determinant in **$[Fe_2Ni_2]^{2+}$**, as expected because the H_4 model is a true singlet, uncontaminated by higher spins. The two additional triplet states for H_4 lie between the high-energy singlet and quintet. The order of these states is retained for variations of the R_2 and R_1 values, and examining how these states evolve from two H_2 molecules in singlet ground states to the H_4 molecule that has a very low-lying singlet helps explain the behavior of the states in the formation of **$[Fe_2Ni_2]^{2+}$** from the two ground state singlet states of **$[FeNi]^+$**.

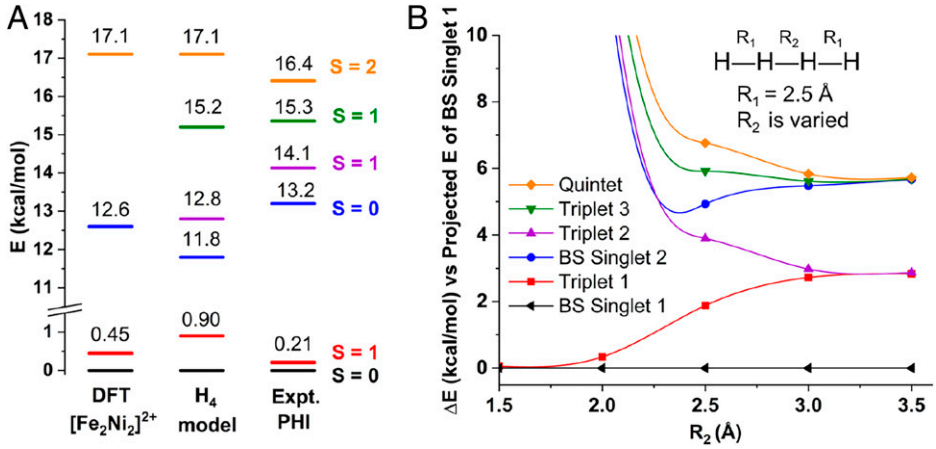

Fig. 10. (*A*) Spin ladders from DFT calculations on the **[Fe_2Ni_2][BArF]$_2$**, the linear H_4 model, and experimental energies obtained from fitting the SQUID data of **[Fe_2Ni_2][BArF]$_2$** with the PHI software. (*B*) Relative energies of the excited spin states in H_4 ($H^{R_1}H^{R_2}H^{R_1}H$) related to distance between atoms when R_1 is set at 2.5 Å and R_2 varies from 1.5 to 3.5 Å.

Fig. 10*B* shows the evolution of the states when two H_2 molecules with fixed R_1 distances of 2.5 Å approach each other starting at $R_2 = 3.5$ Å, where the model is equivalent to two separate H_2 molecules with a GSS at 0.0 kcal/mol (both H_2 molecules in their singlet states), then a pair of higher-energy triplet states around 2.8 kcal/mol (one H_2 molecule in its singlet state and the other H_2 molecule in its triplet state), and finally a singlet, a triplet, and a quintet state grouped together at 5.7 kcal/mol (all the couplings for both H_2 molecules are in their triplet states). As the R_2 distance decreases and the two H_2 molecules are brought together, the two lowest-energy triplets split with one dropping its energy toward the GSS and the other going to higher energies. At $R_1 = R_2 = 2.5$ Å the GSS is at 0.0 kcal/mol, the more stable triplet is at 2.0 kcal/mol, while the less stable one is at 4.0 kcal/mol. At this distance the AFM exchange coupling between each H atom is essentially equal. As R_2 continues to decrease, the coupling between the inner two H atoms becomes larger than the coupling between the outer two H atoms and their closest neighbor, and the splitting between the two triplets increases dramatically with the low-energy one approaching the GSS energy. At this point, the two outer hydrogens experience minimal direct coupling as they are separated by a distance from each other of 6.5 Å, and the increasing strength of the inner two H atoms coupling weakens the outer two H atoms indirect (through bond) coupling. The other states are all moving to significantly higher energy because the electrons of the two inner H atoms involved in these states are triplet coupled. In this context, the docking together of the two interior Ni_{DT}^{+} radical units increases the number of magnetic interactions that leads to a smaller singlet–triplet gap, hence greater magnetism in **[Fe_2Ni_2]$^{2+}$** than that of the individual **[FeNi]$^{+}$** heterobimetallic units.

As mentioned earlier, at least two of the possible J values are required to obtain all six energy levels. Although the magnetic data alone are not sufficient to determine both J values, fixing one from the calculations permits us to calculate the other. Thus, the magnetic susceptibility data were refitted using PHI software under the Heisenberg–Dirac–van Vleck exchange Hamiltonian in Eq. **2**:

$$\hat{H} = -J_1(\hat{S}_1 \cdot \hat{S}_2) - J_2(\hat{S}_1 \cdot \hat{S}_4 + \hat{S}_2 \cdot \hat{S}_3). \qquad [2]$$

The direct orbital overlap within the Ni_2S_2 rhombic core suggests J_1 to be the strongest interaction. In support of this prediction, the dimerization of nickel bis-dithiolene radicals (with Ni–S interdimeric bond distances of ca. 2.5 Å) is reported to result in strong AFM interactions with exchange coupling constants (J) up to $-1{,}876$ cm^{-1} (24, 54). On this premise, satisfactory fits were obtained using $g = 2.0$, $J_1 \approx -3{,}000$ ($-2{,}600$) cm^{-1}, and $J_2 \approx -500$ (-400) cm^{-1}, where the values in parentheses represent parameters for the $BArF^{-}$ solid state and the larger values correspond to the PF_6^{-} analogue, respectively. For the PF_6^{-} salt (DFT vs. PHI energies shown in *SI Appendix*, Fig. S39) the TIP and paramagnetic impurity contributions were 1.3×10^{-4} emu·mol^{-1} and 1.8%, respectively. A large TIP value of 4.3×10^{-3} emu·mol^{-1} contribution was seen for the $BArF^{-}$ (Fig. 10*A* shows energy comparisons) salt with a 4% paramagnetic impurity (*SI Appendix*, Fig. S27). The very large J_1 corresponds to direct exchange interactions within the nickel dithiolene Ni_2S_2 rhomb; a large J_2 value is expected to be also fairly large as calculated for the **[FeNi]$^{+}$** monomer and consistent with other diamagnetic sulfur-bridged bimetallics in butterfly structures with $S = 1/2$ at each metal, e.g., $Fe_2(\mu_2\text{-}S_2(CH_2)_3)(CO)_6$ and **[$Fe_2(NO)_3$]$^{+}$**.

Conclusion

Opportunities for interrogation of species that demonstrate redox activity on alternating positions within stable, isolable synthetic molecular frameworks are not common. Nevertheless, several are identified in active sites of metalloenzymes, especially those involved in reductive processes. The stability of diverse redox levels found in thiolate-S bridged FeNi bimetallics studied here points to the efficacy of bimetallics for sharing, by delocalization through Fe–S–Ni molecular bridges, the burden of changes in charge. In this case, with nickel dithiolene as a Lewis acid receiver unit, the pull on the electrons through the bridging thiolate–sulfur that originated from the iron nitrosyl dithiolate synthon is readily revealed by the ν(NO) IR monitor. Only minor structural changes are needed to accommodate different redox levels; such stability of structures as electrons are added or removed arises from inherent electronic properties of the components of the bimetallic complexes, even in the absence of stabilizing outer sphere cavities that are often operative in metallo–enzyme active sites (EAS). It boosts the claim that small-molecule models of sophisticated EAS might through their design, even with abiotic ligands, compete with metal-based functions within the EAS. It also champions the claim that thiolates, whose nucleophilic activity and deleterious self-reactivity (towards disulfide formation) are "tamed" by transition metals, produce a donating and stabilization effect similar to the classical ligands that facilitate organometallic-like reactivity and catalysis.

Notably, these metalloligands tune the properties of the metal within the receiver unit and also offer the possibility to produce Lewis acid synergistic effects of the adjacent metals.

The greater stability and the more open structure of the nickel dithiolene adduct of (NO)Fe(N_2S_2) as compared to the iron dinitrosyl adduct has inspired a deeper dive into the magnetic properties imbedded within the different redox levels in the Fe–Ni congeners. Especially intriguing is the discrete **[FeNi]$^+$** cation that has strong coupling between the unpaired electron on the $\{Fe(NO)\}^7$ and $[Ni(S_2C_2Ph_2]^{+\bullet}$; a large separation of the ground state singlet and triplet spin levels results in lowered magnetism, essentially diamagnetic behavior. However, the spin-driven dimerization of the **[FeNi]$^+$** cation yields **[Fe_2Ni_2]$^{2+}$** with a flat Ni_2S_2 rhombus or core connector and results in strong coupling between the $Ni_{DT}^{+\bullet}$ units; this dimerization releases the magnetism of remote $\{Fe(NO)\}^7$ and introduces new magnetic interactions. Interpretation of the temperature-dependent magnetic data emphasizes the importance of such interactions and resultant magnetic properties. The magnetic interactions in the dimer reduce the singlet–triplet gap compared to the monomer, resulting in an increase in magnetic moment at room temperature: i.e., two lessor magnets combine to give one of overall greater magnetic power. Interestingly, the metric parameters of the **[Fe_2Ni_2]$^{2+}$** core show slight variations according to counter-cation and, accordingly, slight differences in coupling values. The theoretical H_4 model developed for **[Fe_2Ni_2]$^{2+}$** is likely appropriate for other systems with multiple S = 1/2 sites. An example in this area (55–60) is a vanadyl-based d^1 tetramer, $\{(VO)_4(\mu_3\text{-}OR)_2(\mu_2\text{-}OR)_4\}^{2+}$, with S = 1/2 sites (57) to which this hydrogen model could be applied. Other more complex systems might be amenable to related simple models, which should be helpful when there is too little data to fit a complete magnetic model as in the system described here.

Reduction of **FeNi** occurs at the more accessible $\{Fe(NO)\}^7$ site, resulting in a rare example of a square pyramidal, high-spin (HS) $\{Fe(NO)\}^8$. Mössbauer spectroscopy supported the interpretation that an Fe^{III} oxidation state switches to Fe^{II}. Both iron centers in the respective $\{Fe(NO)\}^{7/8}$ units AFM couple to a HS NO^- ligand. DFT computations support the structural distortions [a large displacement of Fe(NO) out of the N_2S_2 plane] and a triplet state $\{Fe(NO)\}^8$ that is confirmed by SQUID and Evans method magnetometry. Despite the electron density obviously added to $\{Fe(NO)\}^7$, negative charge is distributed to both the μ-SR from the MN_2S_2 donor and the terminal thiolate S of nickel 1,2-ene-dithiolates as displayed in ion pairing to the $[K(18\text{-crown-}6)]^+$ counter-cation and calculated electrostatic potential maps of **FeNi** and **[FeNi]$^-$**.

In conclusion, the pursuit of natural products as targets has enriched the synthetic toolbox of organic chemists for use in many applications. Likewise, our synthetic approach to bimetallic constructs originally inspired by organometallic natural products, such as the hydrogenase EAS, has uncovered paths to unexpected compounds with unique magnetic properties as a result of reduction or oxidation. It is expected that paramagnetic metallodithiolate ligands will be primed for designing new magnetic materials based on the bridging thiolate principles established herein.

Materials and Methods

General Considerations. The following solvents were purified by the MBraun Manual Solvent Purification System with AlcoaF200 activated alumina desiccant, acetonitrile (CH_3CN), dichloromethane (CH_2Cl_2), tetrahydrofuran (THF), hexanes, and diethyl ether (Et_2O). Manipulations and reactions were carried out in anaerobic conditions using standard Schlenk conditions under N_2 atmosphere or in an N_2 atmosphere glovebox. Unless otherwise stated, all reagents were used as received from standard vendors such as Sigma-Aldrich, Tokyo Chemical Industry, and Bean Town chemical. Preparation of *N*,*N*′-dimethyl-*N*,*N*′-bis(2-mercaptoethyl)ethylenediamine (H_2bme-dame), (NO)Fe(bme-dame), and ferrocenium tetrakis[3,5-bis(trifluoromethyl)phenyl]borate (FcBArF) was based on published procedures (25, 29, 61). The supporting electrolyte, [n-Bu_4N][PF_6], $AgNO_3$, KC_8, trifluorotoluene, hexafluorobenzene, 18-Crown-6, and $FcPF_6$ were reagent grade and used as purchased from Sigma-Aldrich. The eicosane (99%) was obtained from Acros Organics.

Infrared spectra were recorded on the Bruker Tensor 37 FTIR spectrometer using a CaF_2 cell with 0.209 mm path length [accurately determined by the fringing effect method (62)]. The monomer/dimer equilibrium was monitored at varying temperatures using an in situ infrared probe attached to a Mettler Toledo iC10 ReactIR spectrometer (path length, 13 μm). The Shimadzu UV-1601PC spectrophotometer was used to collect UV-vis absorption spectra. Electrospray ionization mass spectrometry was performed at the laboratory for Biological Mass Spectrometry at Texas A&M University. Bruker 400 MHz systems were used to record ^1H and ^{19}F NMR spectra. Elemental analysis was performed at the Atlantic Microlab Inc., located in Norcross, GA. Mössbauer spectra were collected on an MS4 WRC low-field spectrometer, and the obtained spectra were fitted using the WMOSS software (both from Science Engineering and Education Co.). An α-Fe foil was used to calibrate the at room temperature.

X-Ray Crystallography. The crystal structures of **FeNi** and **[FeNi]$^-$** were measured at low temperatures (110 K) by a BRUKER Venture X-ray (kappa geometry) diffractometer with a Cu-Iμs X-ray tube (K_α = 1.5418 Å with a potential of 50 kV and a current of 1.0 mA). Single crystals of **[Fe_2Ni_2][BArF]$_2$** and **[Fe_2Ni_2][PF_6]$_2$** were measured using a BRUKER Quest X-ray (fixed-Chi geometry) diffractometer with Mo-Iμs X-ray tube (K_α = 0.71073 Å). Hydrogen atoms were placed in idealized positions and were set riding on the respective parent atoms. All nonhydrogen atoms were refined with anisotropic thermal parameters. Absence of additional symmetry or void was confirmed using PLATON (ADDSYM) (63). The structure was refined (weighted least squares refinement on F^2) to convergence. OLEX2 was employed for the final data presentation and structure plots (64).

Electrochemistry. Cyclic voltammograms were recorded in an airtight three-electrode cell using the CHI600E electrochemical analyzer (CH instruments, Inc.). Measurements were carried out at room temperature in anerobic conditions using CH_3CN or THF as solvent with 0.1 M [^{t}Bu_4N][PF_6] as the electrolyte and 1.0 mM of analyte. All potentials were referenced to the Fc/Fc^+ couple at 0.00 V. A 0.071-cm^2 glassy carbon disk was used as the working electrode, platinum wire was used as the counterelectrode, and the reference electrode was a CH_3CN solution of $Ag/AgNO_3$ in a Vycor-tipped glass tube. When necessary, an alumina–water slurry was used to polish the glassy carbon working electrode throughout the CV experiment; application of a positive pressure of N_2 was used when removing or reinserting the electrode.

Continuous Wave–EPR Measurements. Powder EPR spectra of microcrystalline solid samples of **FeNi**, **[Fe_2Ni_2][PF_6]$_2$**, and **[Fe_2Ni_2][BArF]$_2$** were collected on a continuous wave (CW) X-band (9.39 GHz) ELEXSYS EPR spectrometer at room temperature. CW EPR measurements of **[Fe_2Ni_2][BArF]$_2$** were made on a Bruker ELEXSYS E540 X-band spectrometer equipped with an ER 4116 dual mode resonator, an Oxford ESR900 cryostat, and an Oxford ITC 04 temperature controller for temperature-dependent measurements. Spectra were recorded with microwave field polarizations transverse and parallel to the applied magnetic field with nominal microwave frequencies of 9.65 and 9.41 GHz, respectively. All spectra were collected under nonsaturating conditions with a modulation amplitude of 0.98 mT and a modulation frequency of 100 kHz. Temperature-dependent measurements were recorded using liquid helium at temperatures ranging from 4 to 80 K. CW EPR spectra were processed and simulated using SpinCount (version 6.4.7614.18037), which was developed by Michael Hendrich at Carnegie Mellon University (65). Simulations were calculated via diagonalization of Eq. **3**.

$$\hat{H} = D\left(\hat{S}_z^2 - S(S+1)/3\right) + E(\hat{S}_x^2 - \hat{S}_y^2) + g\mu_B\vec{B}\cdot\hat{S}. \qquad [3]$$

This program computes the powder pattern for a uniform spherical distribution of the magnetic field vector ***B***, and the transition intensities are calculated using Fermi's golden rule (66). The energy between the ground |0> and excited state

$|\pm1>$ spin manifold was obtained by fitting the temperature-normalized signal intensity (S × T) data to a Boltzmann population distribution for a two-level system (Eq. **4**).

$$Intensity\ x\ T\ = \frac{g_i \cdot e^{-\Delta E_i/k_bT}}{\sum_j g_j \cdot e^{-\Delta E_j/k_bT}}. \quad [4]$$

All simulations were generated with consideration of all intensity factors, both theoretical and experimental, to allow for determination of species concentration. The only unknown factor relating the spin concentration to signal intensity was an instrumental factor that is specific to the microwave detection system. However, this was determined by the spin standard, 1 mM Cu(EDTA), prepared from a copper atomic absorption standard solution purchased from Sigma-Aldrich.

Magnetic Measurements. DC magnetic measurements were performed on freshly prepared crushed crystalline samples of **FeNi**, **[Fe$_2$Ni$_2$][PF$_6$]$_2$**, and **[Fe$_2$Ni$_2$][BArF]$_2$** in plastic bags over the temperature range of 2 to 300 K in an applied magnetic field of 1,000 Oe on a Quantum Design SQUID, Model MPMS with 7 T magnet. Magnetic samples of **[FeNi]$^-$** were prepared using crushed crystals in a eicosane matrix inside an NMR tube (high purity). To restrain crystals, the eicosane was heated (40°C) and homogenously dispersed throughout the sample. The NMR tube was then vacuumed sealed with a butane torch. The diamagnetic contribution of the polypropylene bag and eicosane was subtracted from the raw data. Pascal's constants were used to estimate the diamagnetic corrections of the atoms, which were subtracted from the experimental susceptibilities to give the molar paramagnetic susceptibilities (χ_MT). Magnetic (SQUID) data were simulated using the PHI software (50). The temperature dependence of the **[FeNi]$^-$** χ_MT product over the 2 to 300 K range was fitted using the spin Hamiltonian in Eq. **3**.

Synthesis.

(NO)Fe(bme-dame)-NiS$_2$C$_2$Ph$_2$, FeNi. Reactants (NO)Fe(bme-dame) (97 mg, 0.33 mmol) and Ni(CNMe)$_2$-S$_2$C$_2$Ph$_2$ (114 mg, 0.30 mmol) were dissolved in CH_3CN (25 mL). Within 15 min a green precipitate was observed, and the reaction mixture was further stirred for 1 h. The solvent was reduced by half, and excess Et_2O was added to fully precipitate out the product. The green powder was redissolved in minimum CH_2Cl_2 and twice precipitated with addition of Et_2O. In each precipitation step the washings were discarded, and absence of starting material was confirmed with FTIR in CH_2Cl_2. Filtration through a small celite plug was then performed by using CH_2Cl_2 solvent. Dark green crystals of **FeNi** were obtained via vapor diffusion of Et_2O into CH_2Cl_2 solution at 23°C under N_2. The crystals were isolated and repeatedly washed with a 1:2 CH_3CN/Et_2O mixture (5 mL × 3) to afford 145 mg (yield: 80%) of X-ray quality.

[(NO)Fe(bme-dame)-NiS$_2$C$_2$Ph$_2$]$_2$[BArF]$_2$, [Fe$_2$Ni$_2$][BArF]$_2$. A solution of FcBArF (87 mg, 0.083 mmol) in CH_2Cl_2 was added dropwise to a solution of **FeNi** (60 mg, 0.10 mmol) in CH_2Cl_2 at 23°C. The color changed immediately from green to a dark brown, and the solution was further stirred for 15 min. The solvent was then reduced to a minimum followed by addition of excess hexane to precipitate out a black solid. The black solids were washed with copious amounts of hexanes to remove ferrocene. The product was redissolved with Et_2O and filtered through a celite plug. Black X-ray quality crystals of **[Fe$_2$Ni$_2$][BArF]$_2$** were grown by layering the product in Et_2O with pentane at −35°C. The crystals were then washed with Et_2O (5 mL × 3) to afford 108 mg (yield: 90% based on FcBArF).

[(NO)Fe(bme-dame)-NiS$_2$C$_2$Ph$_2$]$_2$[PF$_6$]$_2$, [Fe$_2$Ni$_2$][PF$_6$]$_2$. A solution of $FcPF_6$ (40 mg, 0.12 mmol) in CH_3CN was added dropwise to a solution of **FeNi** (60 mg, 0.10 mmol) in CH_3CN at 23°C. The color changed immediately from green to a dark brown. After further stirring for 15 min, the solvent was reduced to a minimum followed by the addition of excess ether to precipitate a black solid which was triturated with copious amounts of hexanes to remove ferrocene. The product was redissolved in CH_3CN and filtered through a celite plug. Black X-ray quality crystals of **[Fe$_2$Ni$_2$][PF$_6$]$_2$** were obtained by layering the product in CH_3CN with Et_2O at −35°C. The crystals were then washed with Et_2O (5 mL × 3) affording 62 mg (yield: 84% based on **FeNi**).

[(NO)Fe(bme-dame)-NiS$_2$C$_2$Ph$_2$][K(18-c-6)], [FeNi]$^-$. To a 20 mL scintillation vial loaded with **FeNi** (60 mg, 0.10 mmol), KC_8 (20 mg, 0.15 mmol), and 18-c-6 (32 mg, 0.12 mmol), and 10 mL of THF was added at 23°C. The suspension was stirred for 0.5 h during which a color change from green to orange was observed. The THF reaction mixture was then filtered through a cellulose-plugged pipette. Orange X-ray quality crystals of **[FeNi]$^-$** were grown by layering the THF solution with pentane at −35°C. The isolated crystals were washed with pentane to afford 74 mg (yield: 82% based on **FeNi**).

Computational Methodology. DFT calculations were performed in Gaussian 16Revision B.010 (67) with the TPSSTPSS (68) functional. Triple-ζ basis set 6-311++G(d,p) was used for all nonmetals, and 6-311+G was used for metals (69–71). The XRD crystal structures of **FeNi**, **[Fe$_2$Ni$_2$][BArF]$_2$**, **[Fe$_2$Ni$_2$][PF$_6$]$_2$**, and **[FeNi]$^-$** were imported as the starting coordinates for the calculations using GaussView 6.0.16 (72). Single-point calculations were performed on the **[Fe$_2$Ni$_2$]$^{2+}$** species while optimization for the spin ladder and frequency calculations in the gas phase were performed on **FeNi** and **[FeNi]$^-$**. For the monomer **[FeNi]$^+$**, gas phase single-point calculations and optimization/frequency calculations in THF (SMD model) (73) were performed on the monomeric fragment of dimeric **[Fe$_2$Ni$_2$][BArF]$_2$**. For optimization and frequency calculations of the dimer, the phenyl groups were replaced with hydrogen atoms to allow the calculation to converge. All species were confirmed to be minimum energy structures by the absence of imaginary frequencies. Lower-spin BS solutions were converged by repopulation of the converged orbitals from the high-spin solutions. All CI calculations on H_2 and linear H_4 were performed in ORCA version 4.2.1 using a STO-6G basis set (74, 75).

Data Availability. Structure factors and atomic coordinate data have been deposited in the Cambridge Structural Database (CSD) of the Cambridge Crystallographic Data Centre (https://www.ccdc.cam.ac.uk/structures/). The CSD references numbers are as follows: 2123651 (**FeNi**), 2123652 (**[FeNi]$^-$**), 2123653 (**[Fe$_2$Ni$_2$][BArF]$_2$**), and 2123654 (**[Fe$_2$Ni$_2$][PF$_6$]$_2$**). All other study data are included in the article and/or *SI Appendix*.

ACKNOWLEDGMENTS. M.Y.D. acknowledges funding from the NSF (Grant MPS CHE 2102159). M.B.H. and M.Y.D. acknowledge financial support from The Welch Foundation (Grants A-0648 and A-0924, respectively). B.S.P. appreciates financial support from the NIH, Institute of General Medical Sciences (Grant 2 R15 GM117511-01). The authors thank Paul Lindahl for use of Mössbauer instrumentation.

Author affiliations: [a]Department of Chemistry, Texas A&M University, College Station, TX 77843; [b]Department of Chemistry & Biochemistry, Samford University, Birmingham, AL 35229; [c]Chemistry Department, Faculty of Science, Fayoum University, Fayoum 63514, Egypt; [d]Department of Biochemistry and Biophysics, Texas A&M University, College Station, TX 77845; and [e]Department of Chemistry & Biochemistry, University of Alabama, Tuscaloosa, AL 35487

1. R. Eisenberg, H. B. Gray, Noninnocence in metal complexes: A dithiolene dawn. *Inorg. Chem.* **50**, 9741–9751 (2011).
2. J. H. Enemark, R. D. Feltham, Principles of structure, bonding, and reactivity for metal nitrosyl complexes. *Coord. Chem. Rev.* **13**, 339–406 (1974).
3. G. B. Richter-Addo, P. Legzdins, J. Burstyn, Introduction: Nitric oxide chemistry. *Chem. Rev.* **102**, 857–860 (2002).
4. S. Sproules, K. Wieghardt, Dithiolene radicals: Sulfur K-edge X-ray absorption spectroscopy and Harry's intuition. *Coord. Chem. Rev.* **255**, 837–860 (2011).
5. E. I. Stiefel, K. D. Karlin, Eds., *Progress in Inorganic Chemistry, Dithiolene Chemistry: Synthesis, Properties, and Applications* (Wiley, 2004).
6. K. E. Dalle *et al.*, Electro- and solar-driven fuel synthesis with first row transition metal complexes. *Chem. Rev.* **119**, 2752–2875 (2019).
7. R. M. Bullock, *Catalysis without Precious Metals* (Wiley, 2010).
8. A. M. Appel *et al.*, Frontiers, opportunities, and challenges in biochemical and chemical catalysis of CO_2 fixation. *Chem. Rev.* **113**, 6621–6658 (2013).
9. R. M. Bullock *et al.*, Using nature's blueprint to expand catalysis with Earth-abundant metals. *Science* **369**, eabc3183 (2020).
10. W. Lubitz, H. Ogata, O. Rüdiger, E. Reijerse, Hydrogenases. *Chem. Rev.* **114**, 4081–4148 (2014).
11. H. Land, M. Senger, G. Berggren, S. T. Stripp, Current state of [FeFe]-hydrogenase research: Biodiversity and spectroscopic investigations. *ACS Catal.* **10**, 7069–7086 (2020).
12. H. Dobbek, L. Gremer, R. Kiefersauer, R. Huber, O. Meyer, Catalysis at a dinuclear [CuSMo(=O)OH] cluster in a CO dehydrogenase resolved at 1.1-A resolution. *Proc. Natl. Acad. Sci. U.S.A.* **99**, 15971–15976 (2002).
13. R. Hille, J. Hall, P. Basu, The mononuclear molybdenum enzymes. *Chem. Rev.* **114**, 3963–4038 (2014).
14. M. Can, F. A. Armstrong, S. W. Ragsdale, Structure, function, and mechanism of the nickel metalloenzymes, CO dehydrogenase, and acetyl-CoA synthase. *Chem. Rev.* **114**, 4149–4174 (2014).
15. T. C. Pochapsky, S. S. Pochapsky, What your crystal structure will not tell you about enzyme function. *Acc. Chem. Res.* **52**, 1409–1418 (2019).

16. C. Costentin, J.-M. Savéant, C. Tard, Ligand "noninnocence" in coordination complexes vs. kinetic, mechanistic, and selectivity issues in electrochemical catalysis. *Proc. Natl. Acad. Sci. U.S.A.* **115**, 9104–9109 (2018).
17. N. Queyriaux, Redox-active ligands in electroassisted catalytic H^+ and CO_2 reductions: Benefits and risks. *ACS Catal.* **11**, 4024–4035 (2021).
18. J. A. Denny, M. Y. Darensbourg, Metallodithiolates as ligands in coordination, bioinorganic, and organometallic chemistry. *Chem. Rev.* **115**, 5248–5273 (2015).
19. P. Ghosh *et al.*, Structural and electronic responses to the three redox levels of $Fe(NO)N_2S_2$-$Fe(NO)_2$. *Chemistry* **24**, 16003–16008 (2018).
20. C.-H. Hsieh *et al.*, Redox active iron nitrosyl units in proton reduction electrocatalysis. *Nat. Commun.* **5**, 3684 (2014).
21. K. Wang, E. I. Stiefel, Toward separation and purification of olefins using dithiolene complexes: An electrochemical approach. *Science* **291**, 106–109 (2001).
22. B. Garreau-de Bonneval, K. I. Moineau-Chane Ching, F. Alary, T.-T. Bui, L. Valade, Neutral D8 metal bis-dithiolene complexes: Synthesis, electronic properties and applications. *Coord. Chem. Rev.* **254**, 1457–1467 (2010).
23. J. Pitchaimani, S.-F. Ni, L. Dang, Metal dithiolene complexes in olefin addition and purification, small molecule adsorption, H_2 evolution and CO_2 reduction. *Coord. Chem. Rev.* **420**, 213398 (2020).
24. A. I. S. Neves *et al.*, Ni-2,3-thiophenedithiolate anions in new architectures: An in-line mixed-valence Ni dithiolene (Ni4–S12) cluster. *Eur. J. Inorg. Chem.* **31**, 4807–4815 (2011).
25. A. Obanda *et al.*, Expanding the scope of ligand substitution from $[M(S_2C_2Ph_2]$ ($M = Ni^{2+}$, Pd^{2+}, Pt^{2+}) to afford new heteroleptic dithiolene complexes. *Inorg. Chem.* **56**, 10257–10267 (2017).
26. A. Obanda, K. Valerius, J. T. Mague, S. Sproules, J. P. Donahue, Group 10 metal dithiolene bis (isonitrile) complexes: Synthesis, structures, properties, and reactivity. *Organometallics* **39**, 2854–2870 (2020).
27. K. Arumugam *et al.*, Redox-active metallodithiolene groups separated by insulating tetraphosphinobenzene spacers. *Inorg. Chem.* **57**, 4023–4038 (2018).
28. B. S. Lim, D. V. Fomitchev, R. H. Holm, Nickel dithiolenes revisited: Structures and electron distribution from density functional theory for the three-member electron-transfer series $[Ni(S_2C_2Me_2)_2]^{0,1-,2-}$. *Inorg. Chem.* **40**, 4257–4262 (2001).
29. J. L. Hess, H. L. Conder, K. N. Green, M. Y. Darensbourg, Electronic effects of $(N_2S_2)M(NO)$ complexes (M = Fe, Co) as metallodithiolate ligands. *Inorg. Chem.* **47**, 2056–2063 (2008).
30. M. Keilwerth *et al.*, A series of iron nitrosyl complexes $Fe\text{-}NO^{6\text{-}9}$ and a fleeting $Fe\text{-}NO^{10}$ intermediate en route to a metalacyclic iron nitrosoalkane. *J. Am. Chem. Soc.* **141**, 17217–17235 (2019).
31. M. J. Chalkley, J. C. Peters, A triad of highly reduced, linear iron nitrosyl complexes: FeNO(8-10). *Angew. Chem. Int. Ed. Engl.* **55**, 11995–11998 (2016).
32. M. Megnamisi-Belombe, B. Nuber, A new crystalline form of Bis(1,2-diphenyl-1,2-ethenedithiolato)nickel: Asymmetric β-$Ni(dpedt)_2$. *Bull. Chem. Soc. Jpn.* **62**, 4092–4094 (1989).
33. Y. Kitagawa *et al.*, Spin contamination error in optimized geometry of singlet carbene ((1)A1) by broken-symmetry method. *J. Phys. Chem. A* **113**, 15041–15046 (2009).
34. X. Sheng, L. M. Thompson, H. P. Hratchian, Assessing the calculation of exchange coupling constants and spin crossover gaps using the approximate projection model to improve density functional calculations. *J. Chem. Theory Comput.* **16**, 154–163 (2020).
35. P. Comba, S. Hausberg, B. Martin, Calculation of exchange coupling constants of transition metal complexes with DFT. *J. Phys. Chem. A* **113**, 6751–6755 (2009).
36. P. Gütlich, Fifty years of Mössbauer spectroscopy in solid state research–Remarkable achievements, future perspectives. *Z. Anorg. Allg. Chem.* **638**, 15–43 (2012).
37. S. Chatel *et al.*, Structural and spectroscopic characterization of a five-coordinate $\{Fe(NO)\}^6$ complex derived from an iron complex with carboxamido N and thiolato S donors. *Inorg. Chim. Acta* **336**, 19–28 (2002).
38. L. Su, D. Yang, Y. Zhang, B. Wang, J. Qu, Methylene insertion into an Fe_2S_2 cluster: Formation of a thiolate-bridged diiron complex containing an $Fe\text{-}CH_2\text{-}S$ moiety. *Chem. Commun. (Camb.)* **54**, 13119–13122 (2018).
39. C. V. Popescu, S. Ding, P. Ghosh, M. B. Hall, M. Cohara, Mössbauer spectroscopy and theoretical studies of iron bimetallic complexes showing electrocatalytic hydrogen evolution. *Inorg. Chem.* **58**, 7069–7077 (2019).
40. N. Sun *et al.*, S K-edge X-ray absorption spectroscopy and density functional theory studies of high and low spin FeNO7 thiolate complexes: Exchange stabilization of electron delocalization in FeNO7 and FeO28. *Inorg. Chem.* **50**, 427–436 (2011).
41. A. L. Speelman *et al.*, Non-heme high-spin $FeNO^{6\text{-}8}$ complexes: One ligand platform can do it all. *J. Am. Chem. Soc.* **140**, 11341–11359 (2018).
42. A. M. Confer, S. Sabuncu, M. A. Siegler, P. Moënne-Loccoz, D. P. Goldberg, Mononuclear, nonheme, high-spin $FeNO^{7/8}$ complexes supported by a sterically encumbered N_4S-thioether ligand. *Inorg. Chem.* **58**, 9576–9580 (2019).
43. D. F. Evans, The determination of the paramagnetic susceptibility of substances in solution by nuclear magnetic resonance. *J. Chem. Soc.* **1959**, 2003–2005 (1959).
44. K. M. Conner, A. L. Perugini, M. Malabute, S. N. Brown, Group 10 Bis(iminosemiquinone) complexes: Measurement of singlet-triplet gaps and analysis of the effects of metal and geometry on electronic structure. *Inorg. Chem.* **57**, 3272–3286 (2018).
45. F. A. Cotton, J. Su, Z. S. Sun, H. Chen, Preparation and structural characterization of molybdenum acetato phosphine dinuclear $Mo_2Cl_4(OAc)_2(PR_3)_2$ compounds (R = Me, Et) and a comparative study of the singlet-triplet separation for $Mo_2Cl_4(OAc)_2(PEt_3)_2$ with that for $Mo_2Cl_6(dppm)_2$. *Inorg. Chem.* **32**, 4871–4875 (1993).
46. E. I. Solomon, A. B. P. Lever, *Inorganic Electronic Structure and Spectroscopy: Methodology* (Wiley, 2006).
47. A. Blank, H. Levanon, Triplet line shape simulation in continuous wave electron paramagnetic resonance experiments. *Concepts Magn. Reason. A: Bridg. Educ. Res.* **25A**, 18–39 (2005).
48. K. Arumugam *et al.*, Long-range spin coupling: A tetraphosphine-bridged palladium dimer. *Inorg. Chem.* **50**, 2995–3002 (2011).
49. R. M. Clarke *et al.*, Exploiting exciton coupling of ligand radical intervalence charge transfer transitions to tune NIR absorption. *Chem. Sci. (Camb.)* **9**, 1610–1620 (2017).
50. N. F. Chilton, R. P. Anderson, L. D. Turner, A. Soncini, K. S. Murray, PHI: A powerful new program for the analysis of anisotropic monomeric and exchange-coupled polynuclear d- and f-block complexes. *J. Comput. Chem.* **34**, 1164–1175 (2013).
51. M. R. Saber, K. Thirunavukkuarasu, S. M. Greer, S. Hill, K. R. Dunbar, Magnetostructural and EPR studies of anisotropic vanadium *trans*-dicyanide molecules. *Inorg. Chem.* **59**, 13262–13269 (2020).
52. M. P. Shores, J. J. Sokol, J. R. Long, Nickel(II)-molybdenum(III)-cyanide clusters: Synthesis and magnetic behavior of species incorporating [(Me(3)tacn)Mo(CN)(3)]. *J. Am. Chem. Soc.* **124**, 2279–2292 (2002).
53. A. W. Addison, T. N. Rao, J. Reedijk, J. van Rijn, G. C. Verschoor, Synthesis, structure, and spectroscopic properties of copper(II) compounds containing nitrogen–sulphur donor ligands; the crystal and molecular structure of aqua[1,7-Bis(N-methylbenzimidazol-2′-Yl)-2,6-dithiaheptane]copper(II) perchlorate. *J. Chem. Soc., Dalton Trans.* **7**, 1349–1356 (1984).
54. D. Simão *et al.*, Synthesis, structure and physical properties of tetrabutylammonium salts of nickel complexes with the new ligand Dcbdt = 4,5-dicyanobenzene-1,2-dithiolate, $[Ni(Dcbdt)_2]^{z-}$ (z = 0.4, 1, 2). *Eur. J. Inorg. Chem.* **12**, 3119–3126 (2001).
55. H. Chen *et al.*, New linear high-valent tetranuclear manganese-oxo cluster relevant to the oxygen-evolving complex of photosystem II with oxo, hydroxo, and aqua coordinated to a single Mn(IV). *Inorg. Chem.* **44**, 9567–9573 (2005).
56. T. Cauchy, E. Ruiz, S. Alvarez, Magnetostructural correlations in polynuclear complexes: The Fe4 butterflies. *J. Am. Chem. Soc.* **128**, 15722–15727 (2006).
57. W. Plass, Competing magnetic exchange interactions in tetranuclear d(1) systems: Synthesis, structure, and magnetochemistry of a neutral vanadium(IV) complex with a $\{(VO)_4(\mu_3\text{-}OR)_2(\mu_2\text{-}OR)_4\}^{2+}$ core. *Inorg. Chem.* **36**, 2200–2205 (1997).
58. V. V. Pavlishchuk *et al.*, A tetrameric nickel(II) "chair" with both antiferromagnetic internal coupling and ferromagnetic spin alignment. *Angew. Chem. Int. Ed. Engl.* **40**, 4734–4737 (2001).
59. H. B. Lee *et al.*, $S = 3$ ground state for a tetranuclear $Mn^{IV}{}_4O_4$ complex mimicking the S_3 state of the oxygen-evolving complex. *J. Am. Chem. Soc.* **142**, 3753–3761 (2020).
60. H. Sakiyama, A. K. Powell, Magnetic analysis of a tetranuclear octahedral high-spin cobalt(II) complex based on a newly derived magnetic susceptibility equation. *Dalton Trans.* **43**, 14542–14545 (2014).
61. N. G. Connelly, W. E. Geiger, Chemical redox agents for organometallic chemistry. *Chem. Rev.* **96**, 877–910 (1996).
62. B. Stuart, B. George, P. McIntyre, *Modern Infrared Spectroscopy* (Wiley, 1998).
63. A. L. Spek, Single-crystal structure validation with the program PLATON. *J. Appl. Cryst.* **36**, 7–13 (2003).
64. O. V. Dolomanov, L. J. Bourhis, R. J. Gildea, J. A. K. Howard, H. Puschmann, OLEX2: A complete structure solution, refinement and analysis program. *J. Appl. Cryst.* **42**, 339–341 (2009).
65. D. T. Petasis, M. P. Hendrich, Quantitative interpretation of multifrequency multimode EPR spectra of metal containing proteins, enzymes, and biomimetic complexes. *Methods Enzymol.* **563**, 171–208 (2015).
66. C. Cohen-Tannoudji *et al.*, *Quantum Mechanics* (Wiley, 1977).
67. M. J. Frisch *et al.*, *Gaussian 16, Revision C.01* (Gaussian, Inc., Wallingford, CT, 2016).
68. J. Tao, J. P. Perdew, V. N. Staroverov, G. E. Scuseria, Climbing the density functional ladder: Nonempirical meta-generalized gradient approximation designed for molecules and solids. *Phys. Rev. Lett.* **91**, 146401 (2003).
69. A. J. H. Wachters, Gaussian basis set for molecular wavefunctions containing third-row atoms. *J. Chem. Phys.* **52**, 1033–1036 (1970).
70. R. Krishnan, J. S. Binkley, R. Seeger, J. A. Pople, Self-consistent molecular orbital methods. XX. A basis set for correlated wave functions. *J. Phys. Chem.* **72**, 650–654 (1980).
71. A. D. McLean, G. S. Chandler, Contracted Gaussian basis sets for molecular calculations. I. Second row atoms, $Z = 11$–18. *J. Chem. Phys.* **72**, 5639–5648 (1980).
72. R. Dennington, T. A. Keith, J. M. Millam, *GaussView, Version 6* (Semichem Inc., Shawnee Mission, KS, 2016).
73. A. V. Marenich, C. J. Cramer, D. G. Truhlar, Universal solvation model based on solute electron density and on a continuum model of the solvent defined by the bulk dielectric constant and atomic surface tensions. *J. Phys. Chem. B* **113**, 6378–6396 (2009).
74. F. Neese, The ORCA program system. *WIREs Comput. Mol. Sci* **2**, 73–78 (2012).
75. F. Neese, Software update: The ORCA program system, version 4.0. *WIREs Comput. Mol. Sci.* **8**, e1327 (2018).